Image Analysis Method for Estimating Porosity Distribution of Soilcrete

Adriana Luis
Tetra Tech Canada Inc., Vancouver, British Columbia, Canada
Lijun Deng
Department of Civil and Environmental Engineering – University of Alberta, Edmonton, Alberta, Canada

ABSTRACT
A broader research was conducted to investigate the mechanical and physical properties of Edmonton stiff clay treated with ordinary Portland cement and a compound binder of 90% cement and 10% fly ash by weight. Full-scale soilcrete samples were analyzed with computer tomographer (CT) to inspect the pores and fractures after being subjected to triaxial consolidation. Special focus was given to the estimation of porosity distribution by utilizing images obtained with the CT scanner. A new method of analyzing the images was developed to obtain the porosity from the full scale image. The distribution of porosity shows to be more homogeneous on soilcrete containing fly ash, when comparing to soilcrete produced with a cement-only binder. Furthermore, porosities estimated with the developed method show a good agreement with laboratory measured porosity.

RÉSUMÉ
Une recherche plus vaste a été menée afin d'étudier les propriétés mécaniques et physiques de l'argile rigide d'Edmonton traitée avec du ciment ordinaire de Portland et une colle composée de 90% de ciment et de cendres volantes par poids. Des échantillons de béton de sol à grande échelle ont été analysés avec un tomographe cohérente (TC) pour inspecter les pores et les fractures après consolidation triaxiales. Une attention particulière a été accordée à l'estimation de la distribution de la porosité en utilisant des images obtenues avec le scanner CT. Une nouvelle méthode d'analyse des images à été développée pour obtenir la porosité de l'image à grande échelle. La distribution de la porosité se montre plus homogène pour le béton de sol contenant des cendres volantes par rapport au béton de sol produit avec une colle contenant uniquement du ciment. De plus, les porosités estimées avec la méthode développée montrent un bon accord avec la porosité mesuré en laboratoire.

1 INTRODUCTION

Ground improvement techniques, such as deep soil mixing (DSM) and jet grouting are being increasingly used on soils that have poor bearing capacity and are susceptible to settlement in its natural state. These techniques have shown that by adding a cementitious additive (i.e. binder) into the *in-situ* soil in the form of powder or a slurry, the engineering properties of soft soils can be enhanced accordingly. To make this possible, the binder is combined with the right amount of water, to allow for the chemical reactions to occur efficiently, following the concept of Abram's law for hardening of concrete (Miura et al. 2001, Åhnberg et al. 2003, Horpibulsuk et al. 2003, and Lorenzo and Bergado 2004). Once the binder is mixed into the soil, the resulting binder-soil mix is termed as "soilcrete".

The growing need for the DSM to support large superstructures such as oil storage tanks in urban areas may lead to the use of cement mass greater than 20% of the mass of soil solids in order to meet the design specifications for strength. However, published literature related to applications of the DSM using high cement content has been very limited (Miura et al. 2001, Kamruzzaman et al. 2009). Further, there is a lack of research on the effects of confining stress on soilcrete made of stiff clays, because most of the previous research was conducted on cement-treated soft soils, typically in marine environment, pavement subgrade, or contaminant confinement (e.g., Uddin et al. 1997, Banks 2001, Chew et al. 2004, Horpibulsuk et al. 2004, and Kasama et al. 2006). The range of confining stress used in previous research was usually limited to 1 MPa. For an improved understanding of the effects of confinement on properties of soilcrete with high cement content, a greater confining stress should be used.

In addition to the use of destructive loading tests, researchers (e.g., Horpibulsuk et al. 2009, Kamruzzaman et al. 2009) have also relied on images taken with a scanning electron microscope (SEM) to investigate the soil–cement interaction and to quantify the effects of fly ash on the mechanical properties and porosity of soilcrete. Studies carried by Peyton et al. (1992), Waller (2011), and Mao et al. (2012) used computed tomography (CT) scanned images to estimate the porosity and pore size distribution of coal, rocks, and concrete through density measurement based on the grayscale color detected on the images.

Previous research by the authors of the present paper investigated the effects of confining pressures on the mechanical properties of soilcrete with high cement content, by using unconfined compression tests (UCS) (Luis and Deng, 2018) and ICU triaxial tests (Luis and Deng, 2017). For the present paper, image analyses of the specimens were carried by using SEM and CT scan on

soilcrete specimens to assess microstructural changes and porosity. SEM images were taken to investigate the effects of confining pressure and fly ash on the microstructure of soilcrete at the failure plane and outer surfaces. CT scan was performed on selected full-scale soilcrete specimens. The present paper proposes a new method of post-processing the CT scanned images to evaluate the porosity and its distribution along the specimens.

2 MATERIALS AND METHODOLOGY

2.1 Soils and cementitious binders

Natural disturbed soils were collected from a site in eastern Edmonton, where DSM would be performed to support oil storage tanks. The characteristics of the soil are listed in Table 1. Lab testing determined the soil is a low plasticity clay with 33% of sand and a natural water content of 22%. According to the Unified Soil Classification System (USCS) it was classified as a "sandy CL". The oxides composition of the soil is listed in Table 2 and suggest that the clay minerals are illite type, due to the presence of potassium oxide (Holtz et al. 2011).

Table 1. Natural soil characteristics

Quantity	Value
USCS classification	Sandy CL
Liquid Limit	40.9
Plastic Limit	12.5
Plasticity Index	28.4
Natural water content	21.8%
pH	8.1
In-situ s_u (kPa)	63-72
Specific gravity	2.64

Table 2. Oxide composition of binders and soil

	Chemical composition (% by weight)		
Oxide	C [1]	CF [1]	Soil
SiO_2	20.80	19.87	65.66
Al_2O_3	4.20	4.75	10.56
Fe_2O_3	2.40	3.58	8.13
CaO	63.50	62.76	5.21
MgO	2.00	2.54	-
SO_3	3.50	2.67	1.96
Na_2O	-	0.24	-
TiO_2	-	0.44	1.18
K_2O	-	0.18	3.71
P_2O_5	-	0.04	-
SrO	-	0.08	-
Mn_2O_3	-	0.11	-
LOI[2]	2.37	2.32	3.6
Total	98.77	99.58	100

1. C: 100% ordinary Portland cement; CF: 90% ordinary Portland cement and 10% fly ash (class F).
2. LOI: loss on ignition at 440°C for soil and 1000°C for binder C and CF.

Two binders were used for this investigation. The binders were composed by ordinary Portland cement (C binder) or by a mixture of 90% Portland cement and 10% fly ash per weight (CF binder). The chemical composition of the binders is listed in Table 2, which shows about 63% calcium oxide (CaO) in both binders, typical for cement. The addition of small amount of sodium and potassium oxides in the CF binder is due to the presence of fly ash. C and CF binders possess a fines content (% passing 45μu) of 5.9% and 5.03%, respectively. The microstructure of each binder was inspected by using SEM images, and are exhibited in Figure 1, which compares the flaky appearance of cement particles in contrast with the spherical shape of fly ash.

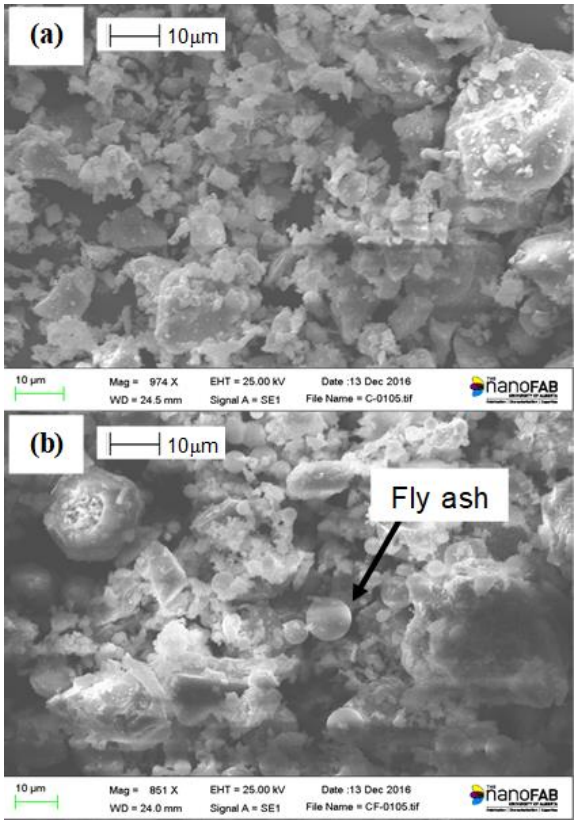

Figure 1. SEM images of binders used for soilcrete. (a) Ordinary Portland cement; (b) 90% ordinary Portland cement with 10% fly per mass of binder.

2.2 Preparation of samples

Soilcrete specimens were produced by combining the cementitious binders with water into a slurry, and then mixing it with the soil. The binder content used for both soilcrete was fixed to 225 kg/m^3 mass of soil with respect to the soil and slurry volume.

The as-built component quantities used in the mix of C and CF type soilcrete are summarized in Table 3. In the present study, the in-place binder content (B_c) used for all

soilcrete was 225 kg/m^3, where B_c is defined in Equation [1] (e.g., Filz et al. 2005, Timoney et al. 2012):

$$B_c = \frac{m_c + m_f}{V_{soil}+V_{slurry}} \quad [1]$$

where: m_c and m_f are the masses of cement and fly ash, respectively, and V_{soil} and V_{slurry} are the volumes of the natural soil and the slurry, respectively. The in-place binder content B_c is a critical parameter used in the design of soilcrete for DSM. A B_c of 225 kg/m^3 is commonly used in the practice and was kept constant for comparison purpose.

The water content (w_c) introduced by Miura et al. (2001), Lorenzo and Bergado (2004) and Horpibulsuk et al. (2005) is defined in Equation [2]:

$$w_c = \frac{m_w + m_{ws}}{m_s} \cdot (100\%) \quad [2]$$

where: m_w is the mass of water in the clay, m_{ws} is the mass of water in the water/binder slurry, and m_s the mass of soil solids. In the present study, w_c was 1.20 times the liquid limit of the natural soil to ensure adequate mixing.

The cement content (C_c) and fly ash content (C_f) used in the binders are defined in Equations [3] and [4]:

$$C_c = \frac{m_c}{m_s} \cdot (100\%) \quad [3]$$

$$C_f = \frac{m_f}{m_s} \cdot (100\%) \quad [4]$$

The total cement content C_T is calculated with Equation [5] (Horpibulsuk et al. 2011):

$$C_T = C_c(1 + 0.75C_f) \quad [5]$$

where the coefficient 0.75 considers the dispersion caused by the fly ash on the cement clusters. In Equation [5], C_f is in a decimal form.

The C_c and C_f for this study were selected in order to achieve C_T in a range of 20.6 to 22.5%. The water content w_c was selected in a range of 53.4 to 54.1% for CF and C soilcrete, respectively. Bruce et al. (2013) show that the best strength development is achieved for w_c/C_T from 1.5 to 3.

The as-built quantities of each element are detailed in Table 3. The binder and tap water were mixed with an electrical blender Warring Commercial (WSB60) to obtain a uniform slurry, and then combined with the soil by mixing the components for about 2 minutes in a Hobart automatic dough mixer (HL200). The soilcrete paste was cast into plastic cylinders of 75 mm diameter and 150 mm length, by pouring layers, and tapping against a hard surface to extract air bubbles. The cylinders were capped with plastic lids and stored in a container at room temperature during the curing time (56 days). These procedures are similar to the methodology proposed by Bruce et al. (2013) for DSM investigations in the US.

Table 3. Binder characteristics.

Property	Binder types	
	C	CF
Binder content (kg/m^3)	225	225
w_c (%)	54.1	53.4
C_c (%)	22.5	20.2
C_f (%)	0	2.2
C_T (%)	22.5	20.6
w_c/C_T	2.4	2.6

2.3 SEM and CT scan procedure

The specimens were allowed to cure for 56 days to allow the development of most of the strength expected at mature age, since the UCS results presented by Luis and Deng (2018) show slower development of strength after 28 days. The specimens were placed into a cylindrical confining cell with a maximum pressure capacity of 4 MPa. The cell fluid is tap water and the pore fluid is deionized water. All the systems were purged prior to testing to avoid entrapped air. The specimen was placed in the confining cell following procedures listed in ASTM (2011). For each binder type, three specimens that were sheared under σ_c' of 0, 500, and 3000 kPa, respectively, were selected for the SEM image analysis. The specimens were dismounted carefully after the triaxial test, and then dried in an oven for 24 hours. Three samples for each specimen were selected from the top, the bottom, and the failure plane, respectively. The samples were sputtered with a thin layer of gold (about 1.6×10^{-5} mm) before placing them into the SEM device. Several images were taken from each sample at various magnifications using the SEM device (ZEISS EVO MA10).

Full-scale specimens were scanned in a computed tomographer, which provided transversal images of each specimen. The images were taken on intervals of 0.3 mm with a resolution of 512 by 512 pixels. Two specimens per each binder type were consolidated at σ_c' of 500 and 3000 kPa, dried in an oven, and then scanned. Additionally, an intact specimen of each binder type, not subject to consolidation, was also dried and scanned. The images from the scanner were later analyzed to determine the effects of increasing confining pressure on the porosity of the soilcrete.

3 IMAGE ANALYSIS

3.1 Scanning Electron Microscope (SEM)

After ICU tests, samples located along the failure plane and other locations of specimens were inspected at several

magnifications with SEM. Figure 2 compares the failure planes in samples of CF soilcrete confined at 0, 500, and 3000 kPa. It is shown that the roughness of the failure surface decreased with increasing σ_c'. This behavior suggests that the reorientation of particles due to the action of high σ_c' leads to a smoother shear failure plane. By comparing images of C and CF soilcrete, it appears that a greater confining pressure was required to reach smoother surfaces in CF soilcrete, when compared to C soilcrete.

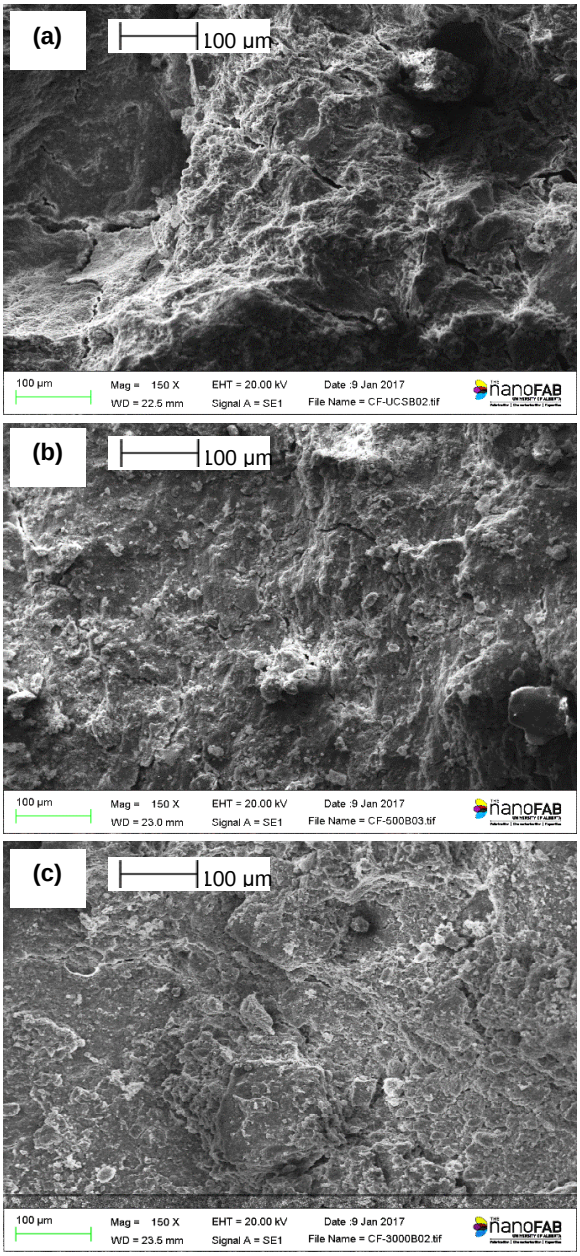

Figure 2. SEM images of failure plane in CF soilcrete subject to different confining pressure: (a) σ_c'= 0 kPa, (b) σ_c' = 500 kPa, and (c) σ_c' = 3000 kPa.

3.2 CT Scan Interpretation

The image-processing software ImageJ (Rasband 1997) was used to analyze CT scan images of specimens, which were scanned on 480 transverse slices at an equal interval of 0.3 mm. The image of each slice is given in grayscale colored pixels, and the color of the pixel varies with the density of the physical element. A darker-colored pixel is interpreted by the software as less density, which implies a more porous element. The size of the element (0.35 mm squared) gives a reasonably good resolution to visualize the voids through the specimen, because it is much less than the specimen diameter (75 mm).

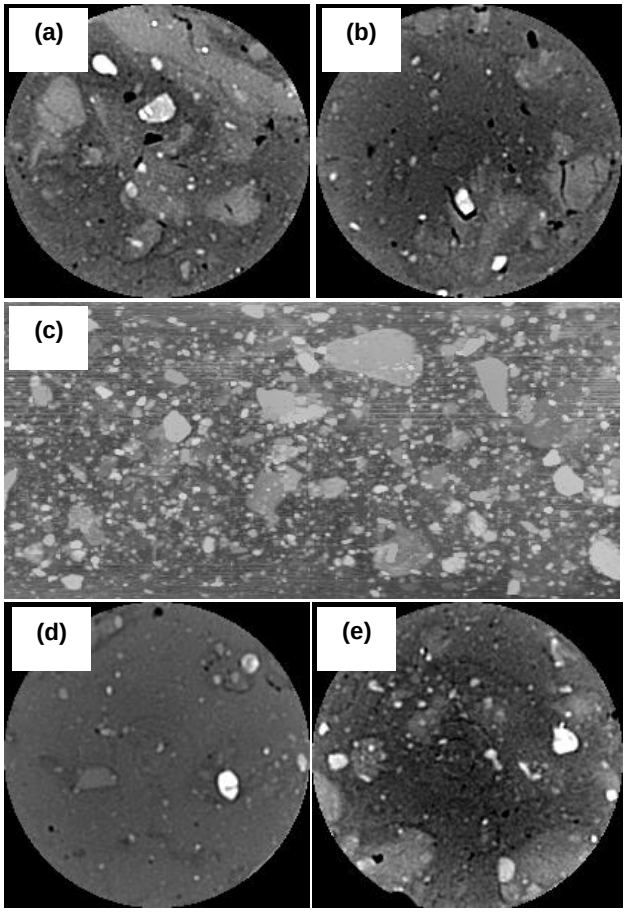

Figure 3. CT scan images of a C soilcrete specimen (a),(b) transverse slice located near the center and bottom of the specimen subject to σ_c' of 500 kPa; (c) longitudinal slice along the central axis generated by the combination of 480 transverse slices for σ_c' of 500 kPa; (d),(e) transverse slice located at the bottom of the samples subject to σ_c' of 0 kPa and σ_c' of 3000 kPa, respectively.

Figures 3a, 3b and 3c contain images of a specimen of soilcrete C confined to 500 kPa along a transverse and a longitudinal section plane, respectively. Figures 3d and 3e show the transverse sections from the bottom of samples

subjected to a confinement of 0 kPa and 3000 kPa. The 100% black patches in the images represent the least density (i.e., cavities) in the soilcrete, whereas the 100% white patches likely represent the zones with more concentrated cement clusters.

For a scanned specimen, the total number of pixels for each grayscale color was summed and displayed in a histogram, as shown in Figure 4. The modal color representing the most frequent color was then determined from the histogram. In this study, the modal color is adopted to separate the porous and filled fractions of the specimen. The pixels on the darker side (left of the modal color) are considered as the voids, which includes the pores, cracks, and the most porous materials. The porosity *n* is then calculated using the pixel color histogram:

$$n = \frac{V_v}{V_T} \quad [6]$$

where: V_v is the voids volume calculated as the total number of pixels in the porous fraction, and V_T is the total volume of the specimen calculated as the total number of pixels in the 480-image sequence.

The porosity *n* could also be estimated from the laboratory-measured mass and volume of specimen using Equation [7]:

$$n = \frac{V_T - \frac{m_s}{G_{seq} \cdot \rho_w}}{V_T} \quad [7]$$

where: V_T is the total volume of the specimen measured after curing and modified by the volumetric strain due to consolidation, G_{seq} is the equivalent specific gravity of the soilcrete, ρ_w is the density of water, and m_s is the mass of the soilcrete solids. G_{seq} was taken as 2.64 for the CF soilcrete and 2.65 for the C soilcrete, according to the specific gravity of clay (2.54), cement (3.15), and fly ash (2.40), and their relative mass contents.

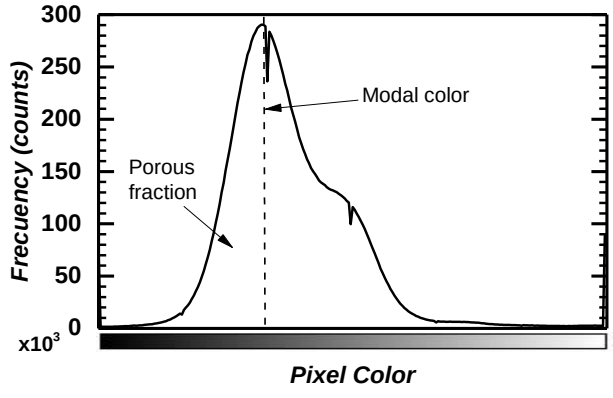

Figure 4. A histogram of the total pixel number for each color in a stack of 480 images of the C soilcrete at σ_c' of 500 kPa.

Figure 5 shows the porosity of six soilcrete specimens after consolidation estimated using Equations [6] and [7]. From the results, it seems that the porosity based on Equation [7] is very consistent with the porosity from the CT scan image analysis. The greatest difference in porosity was 0.04 for a C specimen at σ_c' of 3000 kPa. The simplicity of the proposed method and closeness of results with the laboratory values make it useful in estimating the porosity, when compared to other qualitative methods (e.g., Waller 2011).

To estimate the porosity distribution, images of 25 equally spaced slices in each specimen were extracted from the image sequence. The modal color was estimated from the color frequency histogram corresponding to the whole specimen, and the same modal color was used to define the porous fraction of each of the 25 slices. After defining the porous fraction and total pixel count of each slice, the porosity for each slice was estimated using Equation [6]. The porosity distribution along all specimens are shown in Figure 6.

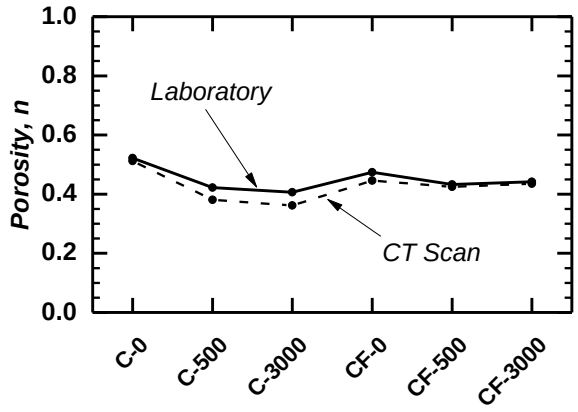

Figure 5. Comparison between porosity estimated from CT scanned images and laboratory calculated porosity.

The porosity profiles show that concentrations of greater porosity occur near one end of the mold. These results suggest that the mixture may be unevenly cast near mold ends, and the top of the specimen accumulated more voids than other locations. The specimen slice with lower porosity may be caused by the accumulation of denser materials such as cement clusters.

The profiles show that the CF soilcrete had more homogeneously distributed porosity than the C soilcrete. The standard deviation (*s*) of the porosity distribution ranged from 0.083 to 0.155 for C specimens. In contrast, *s* of CF specimens varies from 0.075 to 0.099, suggesting a more homogeneous distribution due to the dispersing effect of fly ash on the cement clusters.

4 CONCLUSIONS

The following conclusions may be drawn:

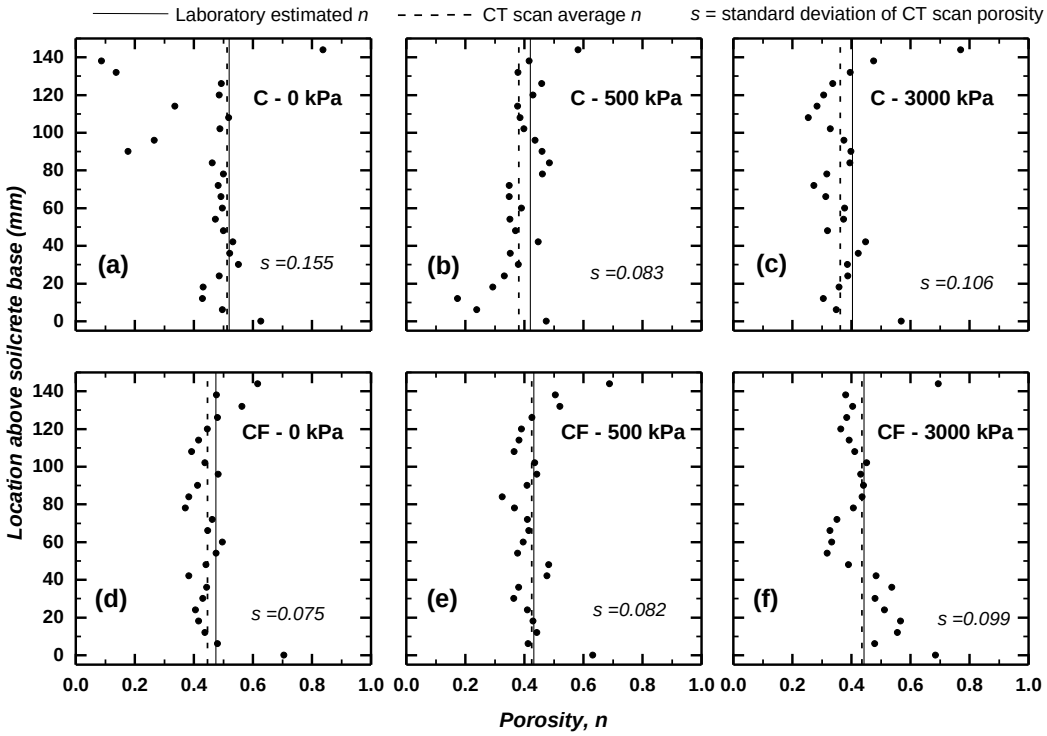

Figure 6. Porosity profiles for specimens consolidated at σ_c' of 0, 500, and 3000 kPa. (a), (b), and (c): C specimens, and (d), (e), and (f): CF specimens.

SEM images showed rough failure surfaces when σ_c' was less than 1 MPa and smoother failure planes with greater σ_c'. in particular, it seems CF specimens had rougher failure surfaces than C specimens at the same σ_c'.

For CT scanned images, the modal color was adopted to differentiate the voids from the solid volume and estimate the porosity. The porosity based on the developed method exhibited a good agreement with porosity estimated from laboratory data.

Porosity was more homogenously distributed in CF specimens than in C specimens, and there were more voids near ends of specimens.

Based on the previous statements, specimens with fly ash inclusions in the binder provide a bonding structure that seems more stable under the effect of confining pressures, compared with the cement only binder. consequently, the more closed nature of the bonding also provides a smaller porosity in CF specimens.

Porosity distributions along the specimens were assessed using a methodology relying solely in image analysis, and the results show a good agreement with laboratory results on both specimen types.

ACKNOWLEDGMENTS

The research is funded by the Natural Sciences and Engineering Research Council of Canada (NSERC) under the Collaborative R&D program (CRDPJ 493088). The authors appreciate Claude Berard from Keller and Dr. Allen Sehn from Hayward Baker Inc. for designing the lab tests.

REFERENCES

ASTM (2011) *Standard Test Method for Consolidated Undrained Triaxial Compression Test for Cohesive Soils*, D4767-11, American Society for Testing and Materials, West Conshohocken, PA.

Åhnberg H, Johansson SE, Pihl H and Carlsson T (2003) Stabilizing effects of different binders in some Swedish soils. *Proceedings of the Institution of Civil Engineers–Ground Improvement*, 7(1), 9-23.

Banks S (2001) *Mechanical characteristics of kaolin-cement mixture, M.Sc. thesis*, Department of Civil and Environmental Engineering, University of Alberta, Edmonton, AB, Canada.

Bruce MEC, Berg RR, Collin JG, Filz GM, Terashi M and Yang DS (2013) *Federal Highway Administration Design Manual: Deep Mixing for Embankment and Foundation Support, Report No. FHWA-HRT-13-046*. Federal Highway Administration. McLean, VA.

Chew S, Kamruzzaman A and Lee F (2004) Physicochemical and engineering behavior of cement treated clays. *Journal of Geotechnical and Geoenvironmental Engineering*, 130(7), 696-706.

Filz GM, Hodges DK, Weatherby, DE and Marr WA (2005) Standardized definitions and laboratory procedures for soil-cement specimens applicable to the wet method of deep mixing. *In Innovations in Grouting and Soil Improvement, ASCE*, Reston, VA., 1-13.

Holtz RD, Kovacs WD and Sheahan TC (2011) An Introduction to Geotechnical Engineering. Upper Saddle River, N.J.: Prentice-Hall.

Horpibulsuk S, Miura N and Nagaraj TS (2003) Assessment of strength development in cement-admixed high water content clays with Abrams' law as a basis. *Geotechnique*, 53(4), 439-444.

Horpibulsuk S, Miura N and Bergado DT (2004) Undrained shear behavior of cement admixed clay at high water content. *Journal of Geotechnical and Geoenvironmental Engineering*, 130(10), 1096-1105.

Horpibulsuk S, Miura N and Nagaraj T (2005) Clay–water/cement ratio identity for cement admixed soft clays. *Journal of Geotechnical and Geoenvironmental Engineering*, 131(2), 187-192.

Horpibulsuk S, Rachan R and Raksachon Y (2009) Role of fly ash on strength and microstructure development in blended cement stabilized silty clay. *Soils and Foundations,* 49(1), 85-98.

Horpibulsuk S, Rachan R and Suddeepong A (2011) Assessment of strength development in blended cement admixed Bangkok clay. *Construction and Building Materials*, 25(4), 1521-1531.

Kamruzzaman AH, Chew SH and Lee FH (2009) Structuration and destructuration behavior of cement-treated Singapore marine clay. *Journal of Geotechnical and Geoenvironmental Engineering*, 135(4), 573-589.

Kasama K, Zen K and Iwataki K (2006) Undrained shear strength of cement-treated soils. *Soils and Foundations*, 46(2), 221-232.

Lorenzo G and Bergado D (2004) Fundamental parameters of cement-admixed clay–new approach. *Journal of Geotechnical and Geoenvironmental Engineering*, 130(10), 1042-1050.

Luis, A, Deng, L. 2017. Engineering Properties of Edmonton Stiff Clay Treated with High Cement Content Using Undrained Triaxial Tests. *Proceedings of the Canadian Geotechnical Conference GeoOttawa 2017,* Taylor and Francis, Ottawa, Ontario, Canada.

Luis, A, Deng, L. 2018. Development of mechanical properties of Edmonton stiff clay treated with cement and fly ash. *International Journal of Geotechnical Engineering,* DOI:10.1080/19386362.2018.1454387.

Mao L, Shi P, Tu H, An L, Ju Y and Hao N (2012) Porosity analysis based on CT images of coal under uniaxial loading. *Advances in Computed Tomography*, 1, 5-10.

Miura N, Horpibulsuk S and Nagaraj TS (2001) Engineering behavior of cement stabilized clay at high water content. *Soils and Foundations*, 41(5), 33-45.

Peyton RL, Haeffner BA, Anderson SH and Gantzer CJ (1992) Applying X-ray CT to measure macropore diameters in undisturbed soil cores. *Geoderma*, 53(3-4), 329-340.

Rasband WS (1997) ImageJ [Computer software for image analysis]. US National Institutes of Health, Bethesda, MD.

Timoney MJ, McCabe BA and Bell AL (2012) Experiences of dry soil mixing in highly organic soils. Proceedings of the Institution of Civil Engineers–Ground Improvement, 165(GI1), 3-14.

Uddin K, Balasubramaniam AS and Bergado DT (1997) Engineering behavior of cement-treated Bangkok soft clay. *Geotechnical Engineering*, 28, 89-119.

Waller JT (2011) *Influence of bio-cementation on shearing behavior in sand using x-ray computed tomography. MSc thesis*, Department of Civil and Environmental Engineering, University of California, Davis, CA.